RSC Advances

PAPER

View Article Online
View Journal | View Issue

Cite this: *RSC Adv.*, 2022, **12**, 30201

Engineering of appropriate pore size combined with sulfonic functionalization in a Zr-MOF with reo topology for the ultra-high removal of cationic malachite green dye from an aqueous medium†

My V. Nguyen, * Hung N. Nguyen, Tuyet A. T. Nguyen and Khang M. V. Nguyen

A Zr-based metal–organic framework with reo topology, denoted as Reo-MOF-1, was fabricated through a solvothermal method capable of efficiently removing the cationic MG dye from an aqueous medium. The effect of pH solution, adsorbent content, adsorption isotherm, and kinetics on the MG capture was observed to determine the optimal conditions. Accordingly, the maximum adsorption capacity of MG over $H^+ \subset$Reo-MOF-1 reaches the value of 2532.1 mg g^{-1} at neutral pH, which is much greater than the published materials. Moreover, the results of the MG process on $H^+ \subset$Reo-MOF-1 fit with the Langmuir isotherm and pseudo second order kinetic model. Hence, MG removal is a chemical adsorption process. Remarkably, $H^+ \subset$Reo-MOF-1 can maintain the uptake for MG at about 94% over eight cycles. The MG adsorption mechanism is interpreted *via* the incorporated analyses and experiments. In detail, Fourier transform infrared spectroscopy (FT-IR), Raman spectroscopy, powder X-ray diffraction (PXRD), and thermogravimetric analysis (TGA-DSC) of MG$\subset$Reo-MOF-1 in comparison with $H^+ \subset$Reo-MOF-1 indicate that the electrostatic attraction and π–π stacking interaction are found *via* the interaction between the cationic MG ions and SO_3^- moieties within MOF as well as the π electron clouds in the benzene ring of the adsorbent and adsorbate, resulting in significant improvement the MG adsorption uptake. These data prove that acidified Reo-MOF-1 possesses promising application as an effective absorbent of toxic dye in practical conditions.

Received 14th September 2022
Accepted 17th October 2022

DOI: 10.1039/d2ra05787e

rsc.li/rsc-advances

1. Introduction

Owing to the rapid growth of urbanization and industrialization, toxic dyes without prior and suitable treatment procedures are directly released into the natural water environment, causing serious consequences for human health and ecosystems in water. Accordingly, these organic dyes cause drawbacks to the photosynthetic process of aquatic life and intense disorders of the human body's immune systems, heart, and skin.[1–3] Hence, solutions for removing toxic dyes from wastewater before discharging are required. Nevertheless, releasing organic dyes is not straightforward due to their complicated structure, leading to research challenges. There are various methods to purge toxic dyes, including advanced oxidation,[4] membrane filtration,[5] catalysis,[6,7] and flocculation.[8] Except for the mentioned methods, adsorption is considered one of the most effective techniques to eliminate toxic dyes from wastewater because of its low cost, convenient operation, eco-friendly and simple design.[9–12] Different absorbents have been prepared and utilized to remove organic dyes from wastewater, such as fiber,[13] orange peel,[14] metal oxide,[15] activated carbon,[16] and zeolite.[17] However, there are many limitations to using these absorbents for removing organic dyes in terms of complex modification, low adsorption ability, slow kinetics, and lack of effective interaction between the adsorption sites and guests. Hence, it is necessary to find novel alternative absorbents for purging toxic dyes and serving the demands in the market. Recently, metal–organic frameworks (MOFs) have emerged as a preeminent candidate for a significant purge of toxic dyes owing to their unique properties such as high porosity, high chemical, and thermal strength, low density, *etc*.[18,19] MOFs are porous materials composed of metal clusters and organic linkers to generate a three-dimensional structure in such a way with diverse topologies. The architecture of MOFs allows the facile modification of the functional groups on the linkers, leading to a broad range of applications in adsorption,[20–22] sensing,[23,24] catalysis,[25,26] and among others.

Malachite green (MG) is a cationic organic dye extensively employed as a precursor in antiseptic agents, antiprotozoal in aquaculture, and fungicide.[27,28] An enormous danger for the discharge of MG into water occurred and severely impacted the

Faculty of Chemistry, Ho Chi Minh City University of Education, Ho Chi Minh City, 700000, Vietnam. E-mail: mynv@hcmue.edu.vn

† Electronic supplementary information (ESI) available: Full synthesis and characterization details of the materials. See DOI: https://doi.org/10.1039/d2ra05787e

habitat of aquatic organisms, including gene mutation, cancer, and cytotoxic.[29] Furthermore, MG possesses a large size and bulky structure (4.3 × 11.4 × 11.4 Å), driving a low MG uptake as using the absorbents with inappropriate pore size and lack of robust interaction between their intrinsic adsorption sites and MG.[30–32] Therefore, a strategy including the pore size engineering combined with functionalized linker in MOFs to remarkably enhance the MG adsorption capacity should be approached. Besides, we published a series of sulfonic-functionalized Zr-based MOFs with ultra-high adsorption levels of cationic methylene blue dye and Pb^{2+} ions *via* the strong electrostatic attraction of their positively charged moieties with the negative charged SO_3^- sites inside Zr-MOF structure.[21,22] With all of this considered, we expect that Reo-MOF-1, owning a suitable pore size and dense SO_3^- moieties packed within the framework, will be employed to eliminate MG from aqueous solution and reach a high uptake of MG *via* efficient synergy.

In this work, we propose a research plan utilizing a Zr-MOF, denoted as Reo-MOF-1, to effectively capture the cationic MG dye through electrostatic interaction and convenient pore size selectivity with the MG size. Consequently, $H^+\subset$Reo-MOF-1 indicated an ultra-high adsorption capacity of 2532.1 mg g^{-1} at a neutral pH, with the uptake, retained without any significant loss after eight cycles. Notably, the structural characteristics and adsorption mechanism of the MG onto $H^+\subset$Reo-MOF-1 were elucidated *via* the adsorption models incorporated with the analysis techniques such as powder X-ray diffraction (PXRD), Raman spectroscopy, Fourier transform infrared spectroscopy (FT-IR), thermogravimetric analysis (TGA-DSC), scanning electron microscopy (SEM), energy-dispersive X-ray (EDX), and transmission electron microscopy (TEM). The obtained data reveal that $H^+\subset$Reo-MOF-1 is the potential candidate to solute the severe threats of the MG dye causing to the water resource.

2. Experimental section

2.1 Materials and methods

All the starting chemicals such as zirconium chloride octahydrate ($ZrOCl_2\cdot 8H_2O$, 99%), fuming sulfuric acid (SO_3 in H_2SO_4, 25%), 2,6-napthalenedicarboxylic acid (H_2NDC, 99%), hydrochloric acid (HCl, 37%), sulfuric acid (H_2SO_4, 98%), formic acid (HCOOH, 96%), *N*,*N*-dimethylformamide (DMF, 98%), and methanol (MeOH, 99%) were obtained from commercial sources without further purification. 4-Sulfonaphthalene-2,6-dicarboxylic acid (H_3SNDC) linker, and DUT-52 were prepared like the reported literature (Section S1†).[21,22]

Powder X-ray diffraction (PXRD) analysis were measured on a Bruker D8 Advance diffractometer using Ni filtered Cu Kα (λ = 1.54718 Å). Fourier transform infrared (FT-IR) spectra were carried out on a spectrophotometer (FT/IR-6600, Jasco) with the Attenuated Total Reflectance sampling method. Raman spectra was collected on a spectrometer (XploRA ONE 532 nm, Horiba). Thermal gravimetric (TG) analysis and differential scanning calorimetry (DSC) curves were conducted using a thermal analyzer at a rate of 10 °C min^{-1} under dry air and argon with the temperature range of 25–800 °C (Labsys Evo 1600 TGA, SETARAM). Scanning electron microscope (SEM) images were obtained using a microscope (FESEM S-4800, Hitachi) combined with energy-dispersive X-ray (EDX) mapping analyzed on an instrument (EDX H-7593, Horiba). Transmission electron microscopy (TEM) images was carried out on a microscope (Jeon 1010, Hitachi). ^{1}H-NMR spectra of linker and digested MOFs were measured on an NMR spectrometer (Advance Neo-600 MHz, Bruker). In particular, MOF materials were digested in 500 μL of DMSO-d_6 solution containing 10 μL of HF. The mixture was then sonicated for 10 minutes before ^{1}H-NMR analysis. UV-Vis spectra were analyzed on a spectrometer (Lambda 25, PerkinElmer).

2.2 Synthesis of DMA⊂Reo-MOF-1

According to the previously reported work,[33] a mixture of H_3SNDC (168 mg, 0.56 mmol) and $ZrOCl_2\cdot 8H_2O$ (196 mg, 0.595 mmol) was introduced to a 50 mL glass bottle containing 7 mL of formic acid and 28 mL of DMF solvent. The mixture was ultrasonicated in 15 min and heated at 120 °C for 72 h. Then, the mixture was cooled to room temperature and centrifuged to obtain a white solid. The solid was washed with DMF for 48 h (30 mL per day) to remove unreacted substances and exchanged with MeOH for 48 h (30 mL per day). Finally, the product was centrifuged, dried, and activated under vacuum at 80 °C for 24 h to acquire a pure sample, namely pristine Reo-MOF-1 (DMA⊂Reo-MOF-1, DMA = dimethylammonium) (83% yield, based on Zr^{4+}). ^{1}H-NMR (digested DMA⊂Reo-MOF-1, DMSO-d_6, 600 MHz): δ = 9.52 (s, 1H), 8.62 (s, 1H), 8.47 (s, 1H), 8.19 (d, 1H), 8.03 (d, 1H), 2.51 (s, H in DMA) (see ESI, Fig. S2†). FT-IR (cm^{-1}, ATR): 3566 (w), 2362 (m), 1648 (m), 1564 (s), 1413 (s), 1352 (s), 1286 (w), 1178 (s), 1045 (s), 991 (m), 925 (m), 845 (m), 767 (s), 648 (s), 621 (s).

2.3 Synthesis of H+⊂Reo-MOF-1

The activated DMA⊂Reo-MOF-1 was immersed in a MeOH/H_2O (= 4/1, *v*/*v*) solution of H_2SO_4 for 48 h (0.2 M H_2SO_4, 5 times per 24 h). The product was collected and washed to pH = 5 with an excess amount of a MeOH/H_2O (= 4/1, *v*/*v*) solution. Continuously, the solid was exchanged with MeOH for 48 h (3 × 10 mL per 24 h), centrifuged, and activated at 80 °C under vacuum for 24 h to obtain a pure $H^+\subset$Reo-MOF-1 (85% yield, based on Zr^{4+}). ^{1}H-NMR (digested $H^+\subset$Reo-MOF-1, DMSO-d_6, 600 MHz): δ = 9.52 (s, 1H), 8.61 (s, 1H), 8.47 (s, 1H), 8.19 (d, 1H), 8.03 (d, 1H) (see ESI, Fig. S3†). FT-IR (cm^{-1}, ATR): 1604 (m), 1554 (m), 1413 (s), 1357 (s), 1285 (w), 1178 (s), 1047 (s), 996 (m), 925 (m), 844 (m), 766 (s), 651 (s), 620 (s).

2.4 Adsorption studies

The pH values of the MG solutions were adjusted by 0.1 M NaOH and HCl solutions in pH range from 1 to 7 using a pH meter. The MG adsorption experiments were conducted at room temperature with a constant stirring rate of 500 rpm. To find the pH point of zero charge (pH_{pzc}) of $H^+\subset$Reo-MOF-1, the material (120 mg) was added to 100 mL of glass flasks containing 50 mL of 0.01 M NaCl solutions with various initial pH ranges (pH_i) from 2 to 11. Next, the mixtures were stirred for 48 h and centrifugated to collect the product. Finally, the final pH value (pH_f) of solutions after stirring was determined on a pH meter. The intersection points between pH_i and pH_f values indicated the pH_{pzc} value.

The remaining concentration of the MG dye after adsorption onto the materials was analyzed by a UV-Vis spectrophotometer with a maximum wavelength of 617 nm. The uptake (%) and adsorption capacity (mg g^{-1}) at equilibrium (q_e) and intervals (q_t) of the MG dye were calculated with the following equations:

$$\text{Uptake} = \frac{C_0 - C_t}{C_0} \times 100 \quad (1)$$

$$q_e = \frac{C_0 - C_e}{m} \times V \quad (2)$$

$$q_t = \frac{C_0 - C_t}{m} \times V \quad (3)$$

where C_o, C_e, C_t (mg L^{-1}) are the concentration of MG at initial and equilibrium, t time. m (mg) symbolizes the absorbent mass and V (mL) is the solution volume.

The absorbent dosage (5–25 mg) of $H^+ \subset$Reo-MOF-1 was introduced into the MG solutions with a concentration of 50 mg L^{-1} to determine the optimal dosage. The adsorption isotherms were carried out with the optimal dosage previously observed, which was added to 100 mL of different initial concentrations of the MG dye (100–1200 mg L^{-1}) and stirred for 24 h. Additionally, the adsorption kinetic models of the MG onto $H^+ \subset$Reo-MOF-1 were surveyed at different intervals from 5 to 120 min. Accordingly, 15 mg of $H^+ \subset$Reo-MOF-1 was introduced to 50 mL of the MG solution (100 mg L^{-1}) at pH = 7.

2.5 Reusability

The regeneration of $H^+ \subset$Reo-MOF-1 was performed by using ethanol as the efficient desorption medium. In detail, the material after accomplished adsorption of the MG dye was collected by centrifugation and immersed in ethanol with stirring for 24 h. To further confirm the complete removal of the MG dye from the material, the filtration was checked without any MG signal indicated in the UV-Vis spectrophotometer. Next, the material was centrifugated and exchanged with ethanol many times. Finally, $H^+ \subset$Reo-MOF-1 was dried, activated at 80 °C under vacuum for 24 h, and utilized for the subsequent experiments.

3. Results and discussion

3.1 Synthesis and characterization of Reo-MOF-1

To fully evaluate the effect of sulfonic moieties and pore size within the material on the adsorption capacity of MG, we have prepared two Zr-based MOF materials with exceptionally high chemical stability, termed DUT-52 and Reo-MOF-1. Herein, the structure of DUT-52 crystallizes in the cubic space group of $Fm\bar{3}m$ with a fcu topology, constructed from 12-connected $Zr_6O_4(OH)_4(COO)_{12}$ clusters and unfunctionalized organic linker of NDC^{2-}.[34] DUT-52 possesses the tetrahedral cage (7.6 Å) and octahedral cage (9.0 Å) (Fig. S1†). Following this feature, DUT-52 material is not favorable for MG adsorption due to insufficient pore window diameter and lack of negatively charged groups. Whereas the framework of Reo-MOF-1 is generated by the addition of defect moieties (bending ligand) into the DUT-52 structure with the connection of 8-connected $Zr_6O_8(H_2O)_8(COO)_8$ clusters and sulfonic-functionalized $SNDC^{3-}$.[33] A network of Reo-MOF-1 with reo topology, incorporating the octahedral and cuboctahedral cages with 9.0 Å and 16.9 Å in diameter, is formed (Fig. 1). It is realized that Reo-MOF-1

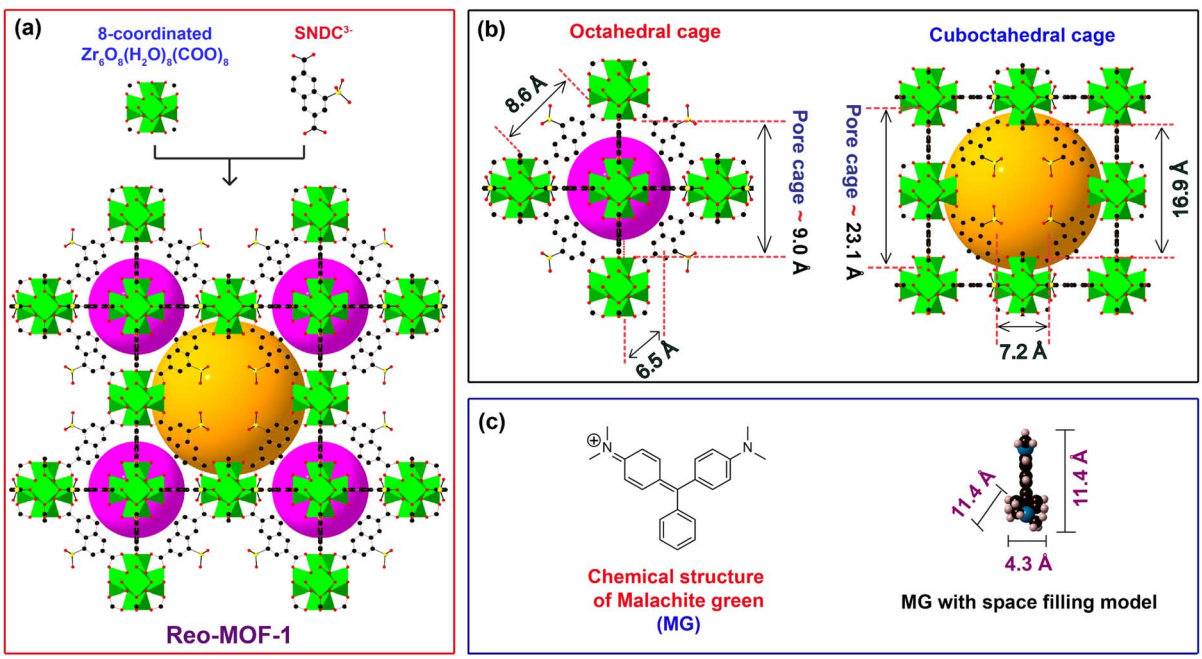

Fig. 1 The structure of $H^+ \subset$Reo-MOF-1 is constructed from 8-connected reo topology and $SNDC^{3-}$ linker (a); the pore window and cage diameter of octahedral and cuboctahedra cage (b); the chemical structure and space filling model of MG (c). Atom colors: Zr, green polyhedra; C, black; O, red; S, yellow; N, blue. Almost H atoms are omitted for clarity.

contains the dense sulfonic groups and suitable pore window size, capable of the effective anchoring of the cationic MG dyes onto the structure *via* electrostatic interactions between the positively charged MG^+ moieties and the negatively charged SO_3^- groups combined with pore size selectivity.

Herein, DUT-52 was fabricated by dissolving $ZrCl_4$ salt and H_2NDC linker into DMF solvent with acetic acid as a modulator to form the crystal nucleation process, heated at 120 °C for 24 h.[34] The pristine Reo-MOF-1 was synthesized from the mixture of $ZrOCl_2 \cdot 8H_2O$ salt and H_3SNDC linker in DMF with the presence of another modulator as formic acid, heated at 120 °C for 72 h, to create a defect structure of DUT-52 with reo net.[33] The phase purity of the as-synthesized Reo-MOF-1 (DMA⊂Reo-MOF-1) sample was confirmed by powder X-ray diffraction (PXRD) analysis, which was in good correspondence with the simulated Reo-MOF-1 (Fig. 2a). Interestingly, there are the appearance of $(CH_3)_2NH_2^+$ (DMA = dimethylammonium) cations during the synthetic process by the decomposition of DMF solvent. The sulfonate groups exist in the anionic forms in Reo-MOF-1 to retain the charge balance with DMA^+ ions inside the whole backbone. This led to a rigid structure capable of maintaining the structural order.

To achieve the convenient space for the adsorption of MG onto Reo-MOF-1, we conducted the ion exchange process between DMA^+ ions and abundant H^+ ions to recover the SO_3H groups within the framework. Noteworthy, DMA⊂Reo-MOF-1 was immersed in an acidic medium (0.2 M of H_2SO_4) to protonate the sulfonate groups entirely and washed with an excess amount of MeOH/H_2O solution to obtain a new freshly made phase. The product was then dried and activated under vacuum at 80 °C for 24 h to give the pure phase of MOF, denoted as H^+⊂Reo-MOF-1.

To inspect whether the DMA ions are totally removed from the structure of Reo-MOF-1, the activated DMA⊂Reo-MOF-1 and H^+⊂Reo-MOF-1 were digested in DMSO-d_6 solution for ^{1}H-NMR analyses. As expected, the DMA peak no longer appears in the digested H^+⊂Reo-MOF-1 compared to the digested DMA⊂Reo-MOF-1 sample (Fig. S2 and S3†). It is noted that the sulfonic moieties in H^+⊂Reo-MOF-1 interact strongly with the solvent molecules through the hydrogen bonding system. These solvent molecules will leave the framework of H^+⊂Reo-MOF-1 during the activation process, causing the loss of the structural periodicity within H^+⊂Reo-MOF-1 due to the high pliability of SO_3H groups. This situation is also found in the reported studies.[21,22,33] However, the crystallinity of the material is recovered when this material is soaked in water (Fig. 2a).

Moreover, the chemical stability of H^+⊂Reo-MOF-1 was affirmed by immersing in water. As a result, the structure of H^+⊂Reo-MOF-1 still maintains after soaking in water for two months, as indicated by the PXRD analysis (Fig. S4†).

The Fourier transform infrared (FT-IR) spectra of DMA⊂Reo-MOF-1, and H^+⊂Reo-MOF-1 are performed. The FT-IR spectroscopy of H^+⊂Reo-MOF-1 reveals the presence of C–O asymmetric and symmetric characteristic bands, appearing at 1604 and 1414 cm^{-1}, respectively (Fig. 2b). Furthermore, the vibration of the sulfonic groups is also found by the broadened peak at 1181 cm^{-1}. In particular, the bands of C–O and SO_3^- groups within DMA⊂Reo-MOF-1 emerged at lower vibrational frequency ranges of 1598, 1411, and 1178 cm^{-1}, respectively. This can be accounted for by the significant interaction between the DMA^+ ions and SO_3^- groups, leading to the decrease of the wavenumber.

To further confirm the characteristics of the materials, thermal gravimetric analysis incorporated with differential scanning calorimetry (TGA-DSC), scanning electron microscopy (SEM) connected with energy-dispersive X-ray (EDX) mapping, and transmission electron microscopy (TEM) analysis were performed on the activated materials. Consequently, TGA-DSC

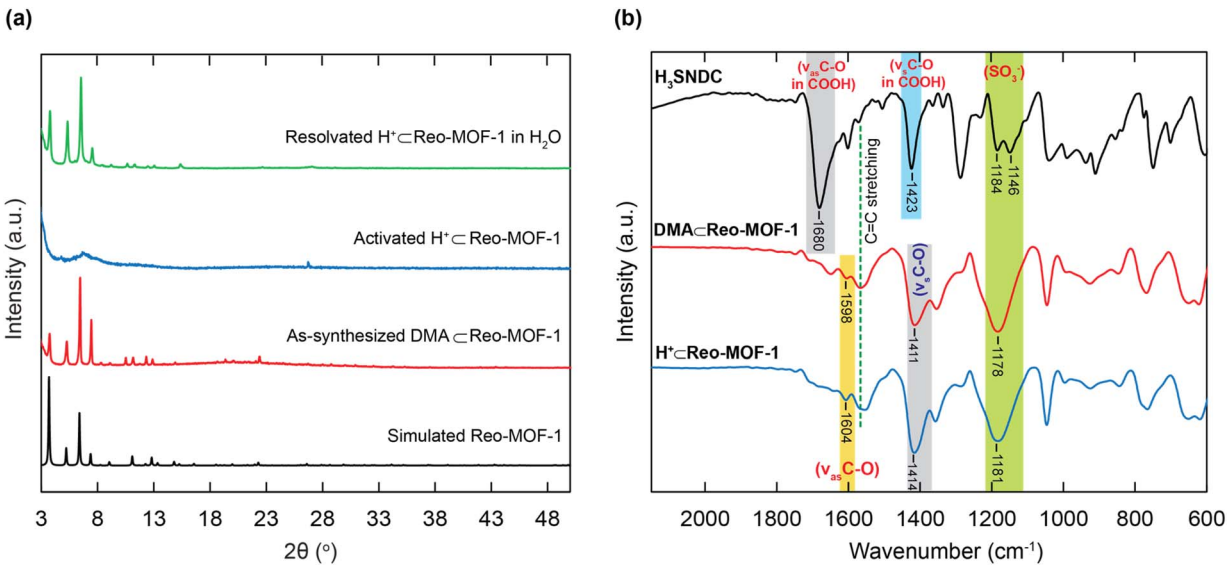

Fig. 2 Powder X-ray diffraction analysis of as-synthesized DMA⊂Reo-MOF-1 (red), activated H^+⊂Reo-MOF-1 (blue), and resolvated H^+⊂Reo-MOF-1 in water (green) in comparison with simulated Reo-MOF-1 (black) (a); Fourier transform infrared spectra of H_3SNDC linker (black), DMA⊂Reo-MOF-1 (red), and H^+⊂Reo-MOF-1 (blue) (b).

curves are carried out under argon and dry air, as demonstrated in Section S5.† The obtained results indicate that the framework of $H^+\subset$Reo-MOF-1 and DMA$\subset$Reo-MOF-1 is thermally stable up to 450 °C with reasonable specific exothermic and endothermic peaks, even in argon and dry air medium. Subsequently, SEM and TEM images show that $H^+\subset$Reo-MOF-1 particles have a prism-like shape and are almost uniform, with an average size of 100–150 nm (Sections S7 and S8†). Especially, EDX spectrum and EDX-mapping are given in Fig. S10,† showing the uniform distribution of C, O, S, and Zr as the elementary components.

To demonstrate the role of relevant pore size engineering combined with SO_3H-functionalized linker within MOFs to the MG adsorption ability, we have conducted a series of complete experiments. In detail, 10 mg each of DUT-52, and $H^+\subset$Reo-MOF-1 are introduced into 50 mL of various MG solutions (20–400 mg L^{-1}). As a consequence, the MG adsorption capacity of $H^+\subset$Reo-MOF-1 reaches a value of 1685.1 mg g^{-1} at the MG initial concentration of 400 mg L^{-1} (Fig. 3a). It is clear to note that the ultra-high MG adsorption capacity onto $H^+\subset$Reo-MOF-1 can be explained by raising the electrostatic interaction between the negatively charged SO_3^- groups inside the backbone and the positively charged MG^+ ions with a compatible pore diameter (Fig. 1b and c). Meanwhile, DUT-52 exhibits a poor adsorption uptake for MG due to the lack of SO_3^- sites within the structure, as well as its inappropriate pore size in comparison with the molecular size of MG (Fig. 3a). Therefore, we select $H^+\subset$Reo-MOF-1 to study the following adsorption experiments in this work.

3.2 Influence of pH

The pH value is an essential factor of the direct effect on the formation of the ion species and surface charges of $H^+\subset$Reo-MOF-1.[35,36] Hence, the experiments have been performed to determine the pH_{pzc} value of the material (see Experimental section). Fig. 3b indicates that the pH_{pzc} value of $H^+\subset$Reo-MOF-1 is 4.3. It is realized that there is a surface charge change from the positive to the negative range with the increase of the solution pH value around the pH_{pzc} value. Next, the solution pH ranges from 1 to 7, impacting the adsorption performance of MG, were surveyed. As given in Fig. 3c, the uptake rate of MG onto $H^+\subset$Reo-MOF-1 reveals a remarkable dependence on the solution pH values. At the pH ranges from 5 to 7, being higher than the pH_{pzc}, the anionic species of $H^+\subset$Reo-MOF-1 formed by the deprotonation of SO_3H groups can efficiently eliminate the MG dyes from the aqueous solution through electrostatic

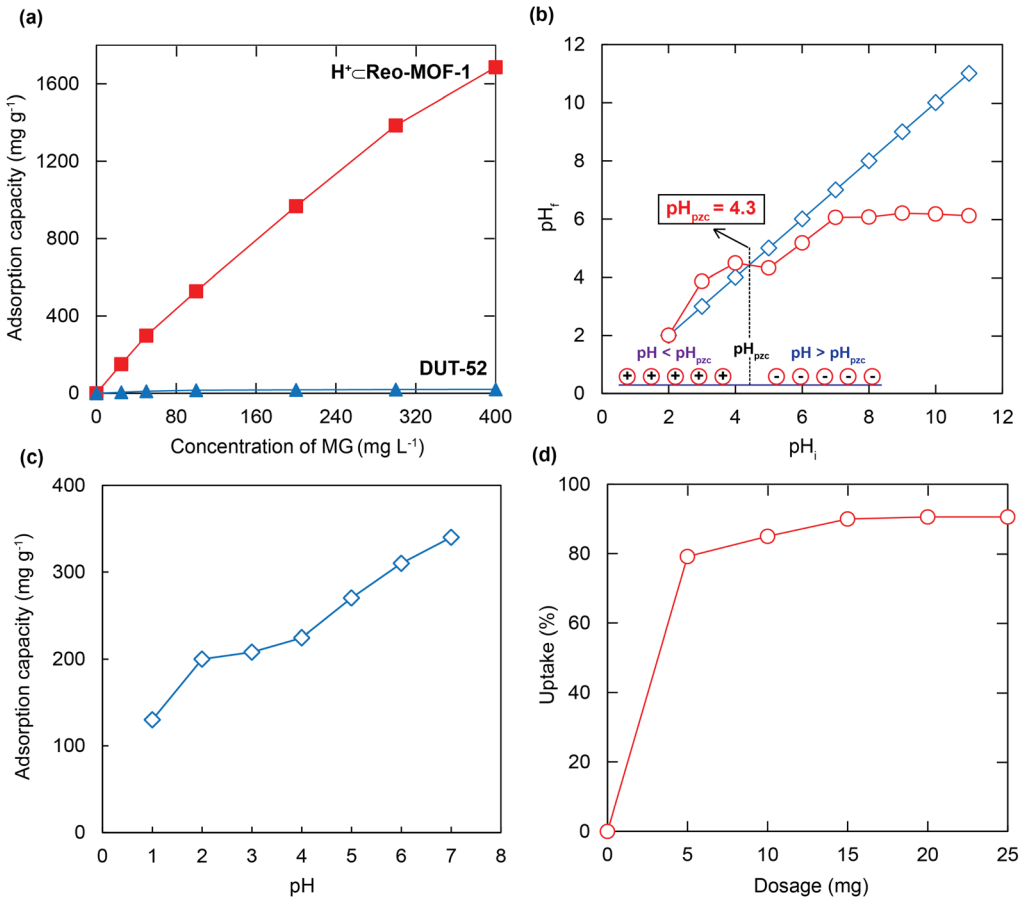

Fig. 3 Dependence of the sulfonic groups and pore size within the structures of DUT-52 and $H^+\subset$Reo-MOF-1 on the MG adsorption capacity (a); the effect of the initial pH on the final pH for determining pH_{pzc} of $H^+\subset$Reo-MOF-1 material (b); influence of solution pH value on the adsorption capacity of MG over $H^+\subset$Reo-MOF-1 (c); effect of $H^+\subset$Reo-MOF-1 content on the MG adsorption uptake (d).

attraction, driving to the high adsorption capacities. Meanwhile, the low uptake levels of MG have occurred at the pH regions from 1 to 4 ($pH < pH_{pzc}$), which can be attributed to the protonation process of SO_3H moieties, leading to the generation of the new $SO_3H_2^+$ species and driving the inner channel wall and the surface of the material charged positively. This causes a considerable repulsion of the cationic moieties such as MG^+, H^+ ions, and $H^+ \subset$ Reo-MOF-1.[22,37,38] The fact shows that the MG ions will easily create the precipitation of the MG carbinol forms and detach from the solution at pH > 7,[39] which causes obstacles to confirming whether the uptake process of MG onto the material or the precipitation of MG has taken. Therefore, we select the best pH value of 7 for the subsequent observations.

3.3 Effect of the material content

To investigate the optimum content of the material for enhancing the interaction between the adsorption sites within $H^+ \subset$ Reo-MOF-1 and the MG ions, the different dosages of activated $H^+ \subset$ Reo-MOF-1 from 5 to 25 mg were added to 50 mL of the MG solution (50 mg L^{-1}) at an optimal pH previously surveyed and stirred for 24 h. As illustrated in Fig. 3d, the adsorption uptake rises sharply from 79 to 92% as the adsorbent content increases from 5 to 25 mg, respectively. This can be ascribed to the rise in the $H^+ \subset$ Reo-MOF-1 dosage, leading to more adsorption spaces and sites for MG removal. As the material's content yields about 15 to 25 mg, the uptake of MG changes inappreciably only by 0.2%, exhibiting the established adsorption equilibrium. Thus, the material dosage of 15 mg is permanently used for the following experiments.

3.4 Adsorption isotherms

To gain insight into the MG adsorption essence of $H^+ \subset$ Reo-MOF-1, the adsorption isothermal models were employed to elucidate the attraction between the MG ions and the adsorbent. Generally, the maximum adsorption capacity is reached when it has insignificantly changed with the rise of the initial adsorbate concentration. Fig. 4a displays the influence of the initial content of MG on the adsorption capacity. It is found that the adsorption quantity is rapidly improved as the initial concentration of MG increases from 50 to 800 mg L^{-1}. During this period, the surface of $H^+ \subset$ Reo-MOF-1 possesses adequate active sites to capture the MG dyes. Besides, the driving force of the mass transfer process is enhanced with the increase of the MG concentration. When the MG concentration rises from 800 to 1200 mg L^{-1}, the adsorption capacity of MG onto $H^+ \subset$ Reo-MOF-1 gains slowly until the equilibrium of the MG uptake is obtained. Herein, the entire active sites within $H^+ \subset$ Reo-MOF-1 are filled, driving a maximum adsorption level of MG.

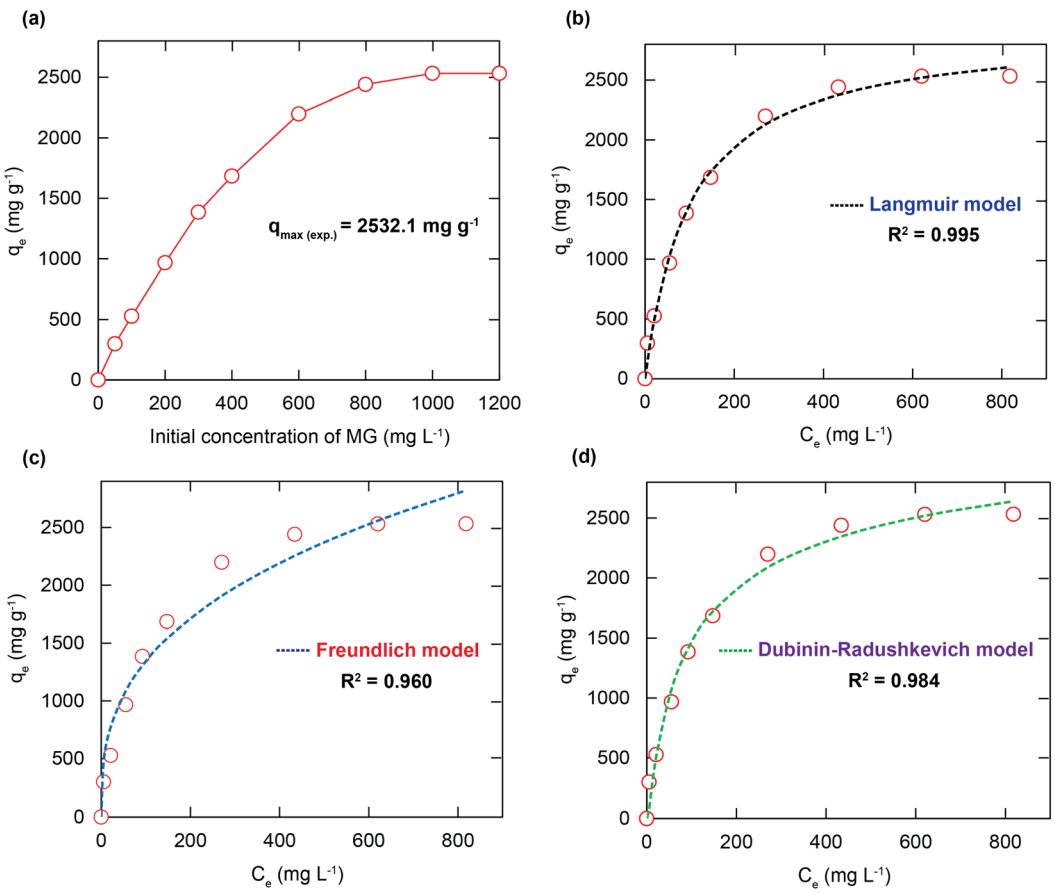

Fig. 4 Effect of the initial concentration of MG on the adsorption capacity of $H^+ \subset$ Reo-MOF-1 (a); fitting results with the adsorption isotherm models: Langmuir (b), Freundlich (c), and Dubinin–Radushkevich (d).

To better interpret the adsorption mechanism of MG onto the material, the adsorption isothermal models such as Langmuir, Freundlich, Dubinin–Radushkevich (DR), and Temkin were utilized. Here, the Langmuir model describes the adsorption equilibrium between the adsorbent and adsorbate in which the sorption takes place on a uniform surface with one adsorbate molecular layer. The Freundlich model supposes that the adsorption happens at the heterogeneous surface with a non-uniform distribution of the adsorption heat over the surface. The DR isotherm is used to depict the adsorption mechanism with the arrangement of the Gaussian energy onto the heterogeneous surface. In comparison, the Temkin model includes a factor with respect to the interaction between adsorbent and adsorbate. This model implies that the adsorption heat of all molecules in the layer would decline non-linearly. The non-linear types of the four isothermal equations are exhibited in eqn (S1)–(S4).†

Table 1 The fitting data specified from the adsorption isothermal models of MG onto $H^+ \subset$ Reo-MOF-1

Isothermal models	Parameters	Value
Langmuir	q_m (mg g^{-1})	2604.1
	K_L (L mg^{-1})	0.0098
	R^2	0.995
Freundlich	$1/n$	0.353
	K_F (mg g^{-1} (L $g^{-1})^{1/n}$)	263.91
	R^2	0.960
DR	K_{DR} (mg g^{-1})	0.181
	R^2	0.984
Temkin	K_T (L mg^{-1})	0.197
	β	4.869
	R^2	0.965

Fig. 4b–d and S15† indicate the nonlinear fitting plots of the adsorption models for the MG adsorption onto $H^+ \subset$ Reo-MOF-1. The fitting data are exhibited in Table 1. The nonlinear fitting coefficient of the Langmuir model ($R^2 = 0.995$) is larger than those of the Freundlich ($R^2 = 0.960$), DR ($R^2 = 0.984$), and Temkin ($R^2 = 0.965$) models. Notably, the theoretical adsorption capacity of MG calculated from the intercept of the Langmuir diagram is 2604.1 mg g^{-1}, which is much close to the experimental value (2533.1 mg g^{-1}). It is suggested that the adsorption monolayer of MG is generated at the boundary between the adsorbate and adsorbent. Also, the parameter derived from the Langmuir model is the separation factor of R_L (determined using eqn (S5)†), which is recognized as an

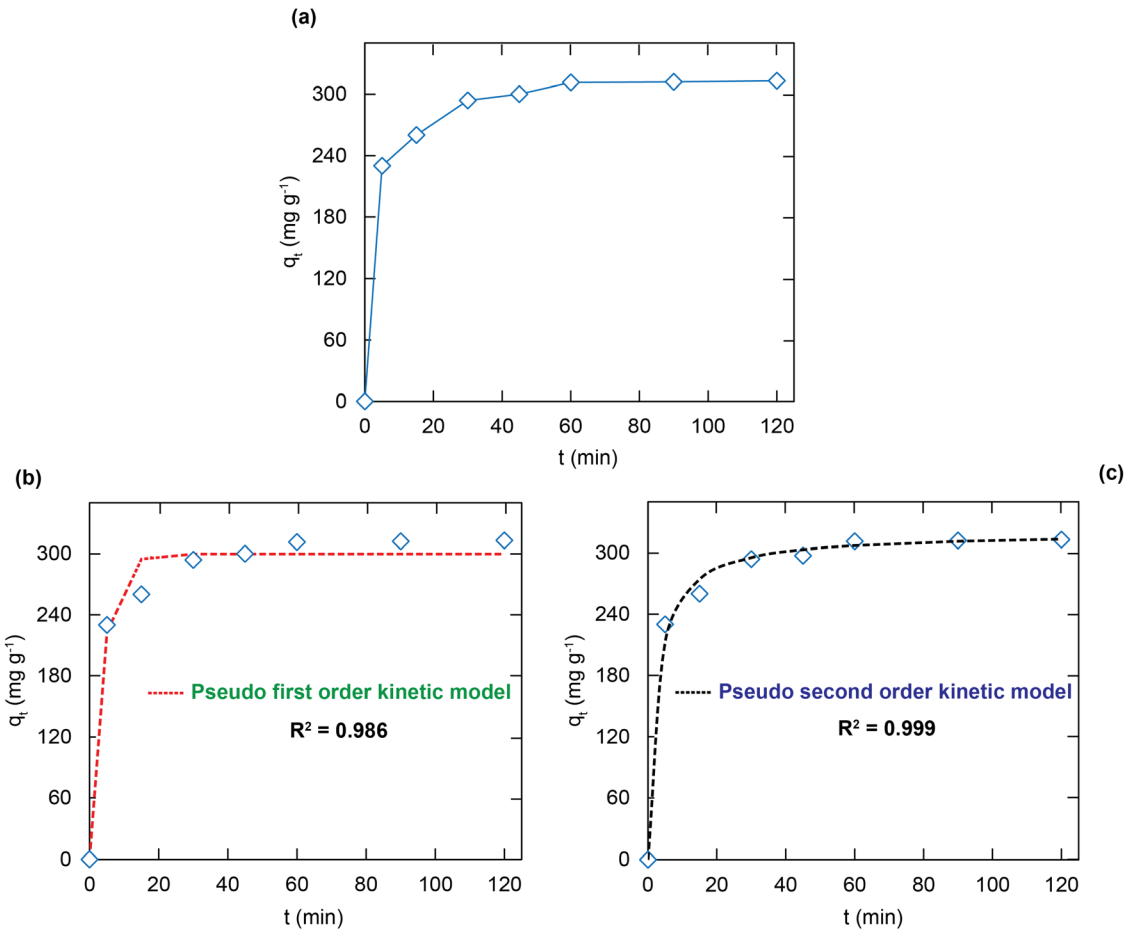

Fig. 5 The kinetic diagram for the adsorption of the MG dye over $H^+ \subset$ Reo-MOF-1 (a); data fitting with the adsorption kinetic model of pseudo first order (b), and second order (c).

important element in evaluating the adsorption favorability.[40] Accordingly, the R_L value is determined to be greater than zero and less than 1 for the distinct initial concentration of MG. This shows that the sorption process of MG onto $H^+\subset$Reo-MOF-1 is most likely to be beneficial and irreversible, which could be attributed to the strong attraction of the active sites within $H^+\subset$Reo-MOF-1 with the positively charged species and π electron clouds of the aromatic rings of the MG dye.[21,22,41] Furthermore, the $1/n$ parameter calculated from the Freundlich model reveals the favorable adsorption process of MG over $H^+\subset$Reo-MOF-1.

3.5 Adsorption kinetics

As given in Fig. 5a, the MG adsorption uptakes over $H^+\subset$Reo-MOF-1 rise promptly during the first 30 min and reach the equilibrium level after 60 min. This fast uptake rate is prominent and wishes for real-life applications to overcome the current limitations of traditional adsorbents. The factors can influence the adsorption property of the material, such as chemical reaction and dispersal rate. Hence, the investigations on the adsorption kinetics were carried out by using the pseudo first order, pseudo second order, and intra-particle diffusion models (see eqn (S6)–(S8)†).

Herein, the hypothesis of the pseudo first order model is that the adsorption rate is decided by the surface. Meanwhile, the pseudo second order model assumes that the adsorption is dominated by the interaction between the functional groups within the material and the adsorbates. The fitting diagrams and parameters are clearly indicated in Fig. 5 and Table 2. The nonlinear fitting coefficient of the pseudo second order ($R^2 = 0.999$) for the MG adsorption onto $H^+\subset$Reo-MOF-1 is larger than that of the pseudo first order model ($R^2 = 0.986$). Thus, the adsorption of MG over $H^+\subset$Reo-MOF-1 is a chemisorption process governed by the exchange or sharing of valence electrons *via* the electrostatic attraction between the positively charged MG ions and the negatively charged SO_3^- groups within the framework as well as the π–π interactions of the electron clouds in the aromatic ring between the adsorbent and adsorbate.[42,43]

Table 2 Pseudo first order, second order model, and intra-particle diffusion model parameters for the MG uptake over $H^+\subset$Reo-MOF-1

Kinetic models	Parameters	Value
Pseudo first order	$q_{e,exp}$ (mg g^{-1})	**313.0**
	$q_{e,cal}$ (mg g^{-1})	298.2
	k_1 (min^{-1})	0.273
	R^2	0.986
Pseudo second order	$q_{e,cal}$ (mg g^{-1})	**320.1**
	k_2 (g mg^{-1} min^{-1})	2300
	R^2	0.999
Intra-particle diffusion		
The first stage	k_{i1} (g mg^{-1} min^{-1})	102.6
	R^2	0.999
The second stage	k_{i2} (g mg^{-1} min^{-1})	19.72
	R^2	0.998
The third stage	k_{i3} (g mg^{-1} min^{-1})	6.667
	R^2	0.995

The results in Fig. S16† exhibit that the MG uptake onto $H^+\subset$Reo-MOF-1 is happened through three stages, with the rate constant values decreasing from k_{i1} to k_{i3}.[44,45] This can be explained by the difference in the MG diffusion rate during the three steps. Accordingly, the MG molecules move rapidly from the solution to the outer surface of $H^+\subset$Reo-MOF-1 material until reaching the saturated state in the first stage. Then in the second stage, the MG molecules enter the internal surface of $H^+\subset$Reo-MOF-1 with an increase in the diffusion resistance. Finally, in the third stage, the MG molecules diffuse slowly into the pore of $H^+\subset$Reo-MOF-1 and strongly interact with the active sites of the framework until the equilibrium is established. It is realized that the third step is slow, but it is not a controlling step of the adsorption process because its straight-line type does not go through the initial position.[46]

3.6 Reusability study

The regeneration of the adsorbent is considered an economic factor in decreasing material costs. Herein, the reusability of $H^+\subset$Reo-MOF-1 in the MG uptake was conducted eight times. The data in Fig. 6 shows that the MG adsorption uptake reaches up to 94% after eight cycles. It is clear that $H^+\subset$Reo-MOF-1 is easily regenerated after the adsorption process without significant loss of adsorption uptake.

Remarkably, the accomplished regeneration of $H^+\subset$Reo-MOF-1 was confirmed by the FT-IR spectra, PXRD, and TEM analyses. Noteworthy, the PXRD patterns of $H^+\subset$Reo-MOF-1 before and after the desorption of MG dye (Fig. S18†) exhibit a high correspondence. The characteristic bands of $H^+\subset$Reo-MOF-1 after the MG desorption are insignificant difference in comparison with the sample before the MG adsorption (Fig. S17†). Moreover, neither morphology nor nanometer-scale changes are observed after recycling, as given in Fig. S11 and S12.† These achieved results demonstrated that $H^+\subset$Reo-MOF-1 material could be utilized as an effectively reusable material in removing toxic dyes from wastewater.

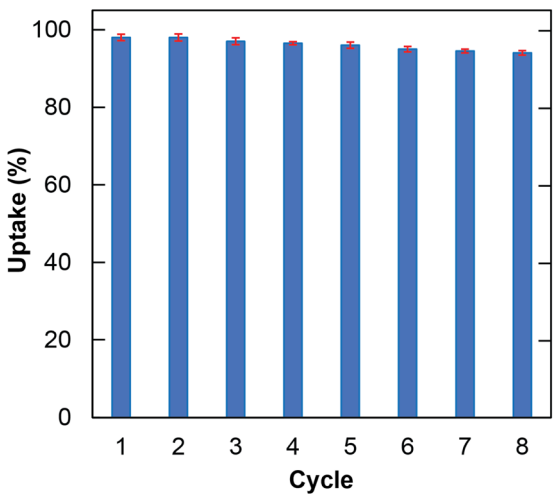

Fig. 6 The reusability of $H^+\subset$Reo-MOF-1 in the MG uptake process.

Table 3 Summary of the maximum MG adsorption capacity of $H^+ \subset$Reo-MOF-1 and the other adsorbents

Material	q_{max} (mg g^{-1})	Ref.
GHBR activated carbon	259.5	30
NaX nanozeolites	347.0	31
Glyricidia sepium	230.5	48
Rice-bran	147.5	49
PMNPs	81.2	50
Coconut AC	91.2	51
Oyster mushroom	32.3	52
Wood apple	80.65	53
Cu-MOFs-2	185.4	54
Cu-MOFs/Fe_3O_4	113.7	55
MIL-53(Al)-NH_2	164.9	56
MIL-68(Al)	153.8	57
NH_2-MIL-101(Al)	274.4	58
ZIF-8	1667.0	59
DUT-52	20.9	**This work**
$H^+ \subset$Reo-MOF-1	**2532.1**	

To further estimate the highlight of this material, the maximum MG adsorption capacity of $H^+ \subset$Reo-MOF-1 was compared with the other adsorption materials (Table 3). As expected, $H^+ \subset$Reo-MOF-1 has the highest adsorption capacity in comparison with the other materials. This can be confirmed that the SO_3^- groups combined with the suitable pore size within $H^+ \subset$Reo-MOF-1 play a vital role in the MG capture.

3.7 Proposed adsorption mechanism

Owing to the presence of SO_3H groups packed densely within the structure incorporated with a suitable pore diameter of $H^+ \subset$Reo-MOF-1, the adsorption mechanism of MG can be considered through the interactions, including electrostatic and π–π interactions. To prove this hypothesis, we conducted a series of additional analyses such as FT-IR spectra, Raman spectroscopy, PXRD, and TGA-DSC.

In detail, the FT-IR spectrum of MG$\subset$Reo-MOF-1 reveals that the characteristic vibrations of the C=O and S=O moved to the lower frequency ranges at 1554 and 1166 cm^{-1}, respectively (Fig. 7a). This result indicates the effective interaction between the SO_3^- moieties and the cationic MG ions, leading to the formation of the chemical bond of the MG^+ ions with sulfonic groups. This phenomenon is in good accordance with the previous studies.[21,22] Furthermore, Raman spectroscopy of

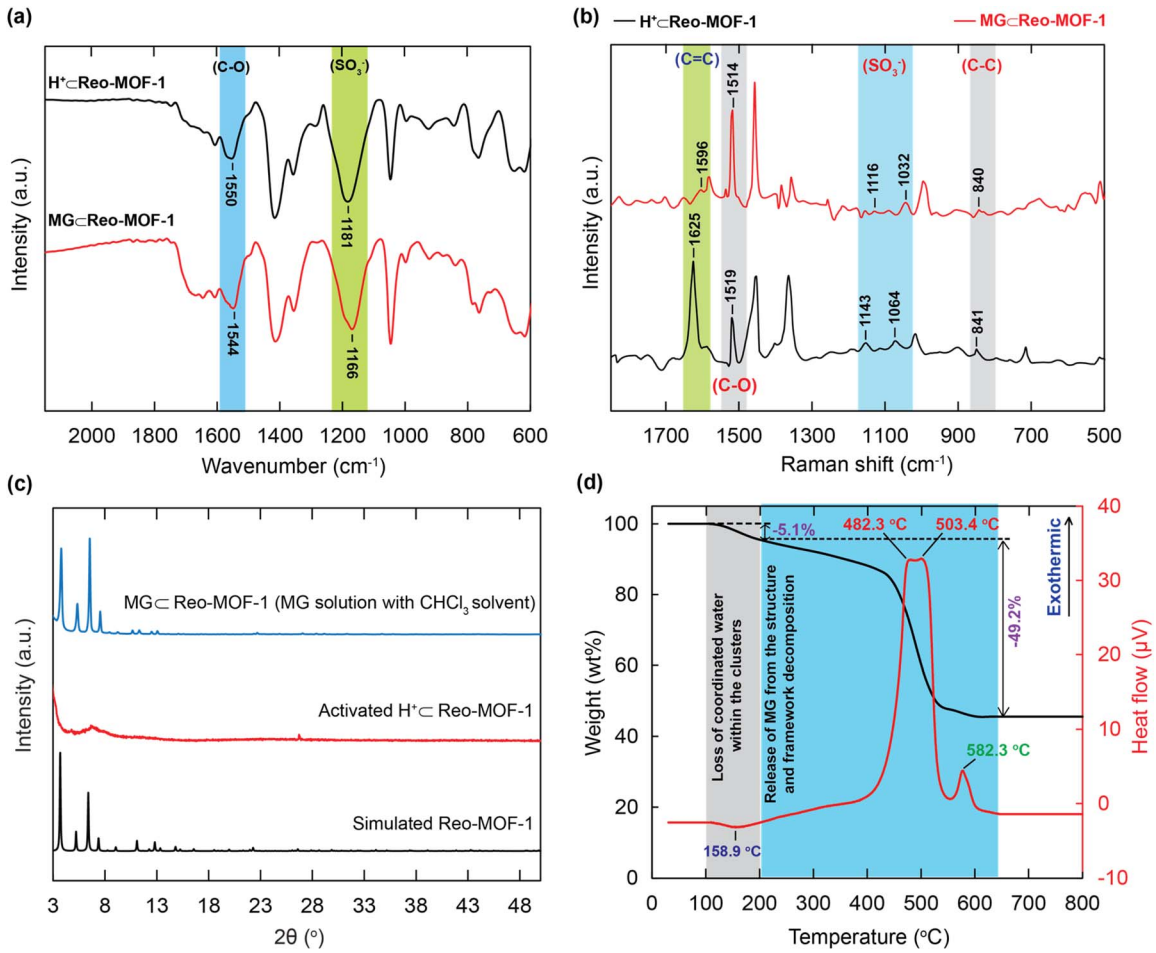

Fig. 7 Fourier transform infrared spectroscopy of MG$\subset$Reo-MOF-1 (red) as compared to $H^+ \subset$Reo-MOF-1 (black) (a); Raman spectroscopy of MG$\subset$Reo-MOF-1 (red) in comparison with $H^+ \subset$Reo-MOF-1 (black) (b); powder X-ray diffraction analysis of MG$\subset$Reo-MOF-1 (MG solution with $CHCl_3$) (blue), activated $H^+ \subset$Reo-MOF-1 (red) in comparison with simulated Reo-MOF-1 (black) (c); TGA diagram (black) and DSC curve (red) of activated MG$\subset$Reo-MOF-1 (d).

MG⊂Reo-MOF-1 is measured and illustrated in Fig. 7b. The new bands are also found at 1596, 1116, and 1032 cm^{-1}, corresponding with the vibrational modes of C=O and S=O, which present in the MG⊂Reo-MOF-1 spectrum, but are appeared at different positions in the H^+⊂Reo-MOF-1 range. This again proves the electrostatic attraction of the negatively charged SO_3^- sites with the positively charged MG ions. Particularly, the signal derived from the C=C vibration in the benzene ring of MG⊂Reo-MOF-1 emerges at another position of 1154 cm^{-1} compared to H^+⊂Reo-MOF-1. It can be supposed that the π–π interactions are generated by the attraction between the conjugated planar of the MG molecules and the channel wall of the material.[21,47]

To further demonstrate the π–π interactions within the framework, H^+⊂Reo-MOF-1 is immersed in the MG solution with chloroform as a non-polar solvent. Herein, we use chloroform solvent for preparing the MG solution to facilitate the generation of the neutral forms of the MG dye and Reo-MOF-1. In fact, the structural order of the activated H^+⊂Reo-MOF-1 sample is lost during activation by the high flexibility of sulfonic groups.[33] Hence, we wish that if the MG molecules are successfully entered into the framework of Reo-MOF-1, its architecture will remain after activation. The PXRD analyses are performed to evaluate whether the MG dyes are anchored inside the structure of Reo-MOF-1. As a result, the PXRD pattern of activated MG⊂Reo-MOF-1 (soaked in the MG solution with chloroform solvent) is in good agreement with the simulated Reo-MOF-1. This can confirm that the neutral MG molecules are absorbed onto the backbone of H^+⊂Reo-MOF-1 *via* π–π interactions (Fig. 7c).

In addition, the presence of the MG molecules within H^+⊂Reo-MOF-1 was inspected by the TGA curve under dry air. As given in Fig. 7d, the TGA diagram and DSC curve exhibit a weight loss of 5.1 wt% from room temperature to 200 °C, corresponding to a maximum endothermic peak at 158.9 °C. This is attributed to the release of coordinated water within the clusters. From 200 to 650 °C, a steep drop appeared and confirmed the loss of the MG molecules from the structure and the framework decomposition, which are clearly illustrated by the considerable exothermic signals at 482.3, 503.4, and 582.3 °C.

4. Conclusion

In summary, a Zr-based MOF with reo topology containing the dense distribution of SO_3H groups combined with relevant pore window diameter was successfully synthesized and studied for its adsorption property of the MG uptake. It is noted that the maximum adsorption capacity for the MG dyes over H^+⊂Reo-MOF-1 is achieved to be 2532.1 mg g^{-1} at a neutral pH. To the best of our knowledge, this value is much higher than the previously reported materials in the MG uptake. The data from the adsorption isothermal and kinetic models reveal that the MG removal is highly correlated with the Langmuir isotherm and the pseudo second order models, which proposed a chemical process during the MG uptake. Additionally, the recycling experiments indicate notable adsorption in reusing the material for eight cycles. Especially the adsorption mechanism is elucidated through the incorporated experiments and analyses. The results show that the adsorption mechanism can be considered *via* the electrostatic and π–π interactions. These findings demonstrate that the Reo-MOF-1 material has a significant promise to be used as a potential adsorbent for MG removal from an aqueous medium.

Author contributions

M. V. N. formulated this project. M. V. N., H. N. N., T. A. T. N., K. M. V. N. synthesized the materials and collected the PXRD analyses, FT-IR spectra, and TGA-DSC analyses. M. V. N. analyzed all experimental data. M. V. N. wrote the paper and all authors contributed to revising it. All authors have approved the final version of the manuscript.

Conflicts of interest

The authors maintain that they have no conflict of interest for this communication.

Acknowledgements

This work was supported by Ho Chi Minh City University of Education, Ho Chi Minh City, Vietnam, through Grant No. CS.2021.19.22.

Notes and references

1 Y. C. Wong, Y. S. Szeto, W. H. Cheung and G. McKay, Adsorption of acid dyes on chitosan-equilibrium isotherm analyses, *Process Biochem.*, 2004, **39**, 693–702.
2 M. T. Yagub, T. K. Sen, S. Afroze and H. M. Ang, Dye and its removal from aqueous solution by adsorption: a review, *Adv. Colloid Interface Sci.*, 2014, **209**, 172–184.
3 H. Xue, Q. Chen, F. Jiang, D. Yuan, G. Lv, L. Liang, L. Liu and M. Hong, A regenerative metal-organic framework for reversible uptake of Cd(ii): from effective adsorption to in situ detection, *Chem. Sci.*, 2016, **7**, 5983–5988.
4 S. Wu, Y. Lin, C. Yang, C. Du, Q. Teng, Y. Ma, D. Zhang, L. Nie and Y. Zhong, Enhanced activation of peroxymonosulfate by $LaFeO_3$ perovskite supported on Al_2O_3 for degradation of organic pollutants, *Chemosphere*, 2019, **237**, 124478.
5 G. Yang, D. Zhang, G. Zhu, T. Zhou, M. Song, L. Qu, K. Xiong and H. Li, A Sm-MOF/GO nanocomposite membrane for efficient organic dye removal from wastewater, *RSC Adv.*, 2020, **10**, 8540–8547.
6 M. A. Ahsan, A. R. P. Santiago, A. N. Nair, J. M. Weller, M. F. Sanad, D. J. V. Rosales, C. K. Chan, S. Sreenivasan and J. C. Noverona, Metal-organic frameworks-derived multifunctional carbon encapsulated metallic nanocatalysts for catalytic peroxymonosulfate activation and electrochemical hydrogen generation, *Mol. Catal.*, 2020, **498**, 111241.
7 M. A. Ahsan, A. R. P. Santiago, M. F. Sanad, J. M. Weller, O. F. Delgado, L. A. Barrera, V. M. Rojas, B. A. Tenorio,

C. K. Chan and J. C. Noveron, Tissue paper-derived porous carbon encapsulated transition metal nanoparticles as advanced non-precious catalysts: carbon-shell influence on the electrocatalytic behaviour, *J. Colloid Interface Sci.*, 2021, **581**, 905–918.

8 K. Guo, B. Gao, X. Tian, Q. Yue, P. Zhang, X. Shen and X. Xu, Synthesis of polyaluminium chloride/papermaking sludge-based organic polymer composites for removal of disperse yellow and reactive blue by flocculation, *Chemosphere*, 2019, **231**, 337–348.

9 L. Huang, X. Weng, Z. Chen, M. Megharaj and R. Naidu, Green synthesis of iron nanoparticles by various tea extracts: comparative study of the reactivity, *Spectrochim. Acta, Part A*, 2014, **130**, 295–301.

10 N. Wang, Y.-F. Wang, A. M. Omer and X.-K. Ouyang, Fabrication of novel surface-imprinted magnetic graphene oxide-grafted cellulose nanocrystals for selective extraction and fast adsorption of fluoroquinolones from water, *Anal. Bioanal. Chem.*, 2017, **409**, 6643–6653.

11 T. M. Alslaibi, I. Abustan, M. A. Ahmad and A. A. Foul, A review: production of activated carbon from agricultural by products via conventional and microwave heating, *J. Chem. Technol. Biotechnol.*, 2013, **88**, 1183–1190.

12 T. Wu, X. Cai, S. Tan, H. Li, J. Liu and W. Yang, Adsorption characteristics of acrylonitrile, p-toluenesulfonic acid, 1-naphthalenesulfonic acid and methyl blue on graphene in aqueous solutions, *Chem. Eng. J.*, 2011, **173**, 144–149.

13 K. Porkodi and K. V. Kumar, Equilibrium, Kinetics and Mechanism Modeling and Simulation of Basic and Acid Dyes Sorption onto Jute Fiber Carbon: Eosin Yellow, Malachite Green and Crystal Violet Single Component Systems, *J. Hazard. Mater.*, 2007, **143**, 311–327.

14 R. Sivaraj, C. Namasivayam and K. Kadirvelu, Orange Peel as an Adsorbent in the Removal of Acid Violet 17 (Acid Dye) from Aqueous Solutions, *Waste Manage.*, 2001, **21**, 105–110.

15 K. Y. Kumar, H. B. Muralidhara, Y. A. Nayaka, J. Balasubramanyam and H. Hanumanthappa, Low-cost synthesis of metal oxide nanoparticles and their application in adsorption of commercial dye and heavy metal ion in aqueous solution, *Powder Technol.*, 2013, **246**, 125–136.

16 P. K. Malik, Dye removal from wastewater using activated carbon developed from sawdust: adsorption equilibrium and kinetics, *J. Hazard. Mater.*, 2004, **113**, 81–88.

17 E. Alver and A. Ü. Metin, Anionic dye removal from aqueous solutions using modified zeolite: adsorption kinetics and isotherm studies, *Chem. Eng. J.*, 2012, **200–202**, 59–67.

18 Q. L. Zhu and Q. Xu, Metal-organic framework composites, *Chem. Soc. Rev.*, 2014, **43**, 5468–5512.

19 H. C. Zhou, J. R. Long and O. M. Yaghi, Introduction to metal-organic frameworks, *Chem. Rev.*, 2012, **112**, 673–674.

20 R. M. Rego, G. Sriram, K. V. Ajeya, H. Y. Jung, M. D. Kurkuri and M. Kigga, Cerium based UiO-66 MOF as a multipollutant adsorbent for universal water purification, *J. Hazard. Mater.*, 2021, **416**, 125941.

21 T. T. M. Bui, L. T. Nguyen, N. P. H. Pham, C. C. Tran, L. T. Nguyen, T. A. Nguyen, H. N. Nguyen and M. V. Nguyen, A new approach for ultra-high adsorption of cationic methylene blue in a Zr-sulfonic-based metal–organic framework, *RSC Adv.*, 2021, **11**, 36626–36635.

22 C. C. Tran, H. C. Dong, V. T. N. Truong, T. T. M. Bui, H. N. Nguyen, T. A. T. Nguyen, N. N. Dang and M. V. Nguyen, Enhancing the remarkable adsorption of Pb^{2+} in a series of sulfonic-functionalized Zr-based MOFs: a combined theoretical and experimental study for elucidating the adsorption mechanism, *Dalton Trans.*, 2022, **51**, 7503–7516.

23 L. Yang, C. Lian, X. Li, Y. Han, L. Yang, T. Cai and C. Shao, Highly selective bifunctional luminescent sensor toward nitrobenzene and Cu^{2+} ion based on microporous metal-organic frameworks: synthesis, structures, and properties, *ACS Appl. Mater. Interfaces*, 2017, **9**, 17208–17217.

24 L. E. Kreno, K. Leong, O. K. Farha, M. Allendorf, R. P. V. Duyne and J. T. Hupp, Metal-organic framework materials as chemical sensors, *Chem. Rev.*, 2012, **112**, 1105–1125.

25 M. V. Nguyen, H. C. Dong, V. T. N. Truong, H. N. Nguyen, L. C. Luu, N. N. Dang and T. A. T. Nguyen, A new porphyrinic vanadium-based MOF constructed from infinite $V(OH)O_4$ chains: syntheses, characterization and photoabsorption properties, *New J. Chem.*, 2022, **46**, 632–641.

26 H. Liang, X. Jiao, C. Li and D. Chen, Flexible self-supported metal-organic framework mats with exceptionally high porosity for enhanced separation and catalysis, *J. Mater. Chem. A*, 2018, **6**, 334–341.

27 S. Srivastava, R. Sinha and D. Roy, Toxicological effects of malachite green, *Aquat. Toxicol.*, 2004, **66**, 319–329.

28 S. J. Culp and F. A. Beland, Malachite green: a toxicological review, *J. Am. Coll. Toxicol.*, 1996, **15**, 219–238.

29 C. Fernandes, V. S. Lalitha and K. V. K. Rao, Enhancing effect of malachite green on the development of hepatic preneoplastic lesions induced by nitrosodiethylamine in parts, *Carcinogenesis*, 1991, **12**, 839–845.

30 A. A. Ahmad, M. A. Ahmad, N. K. E. Yahaya and J. Karim, Adsorption of malachite green by activated carbon derived from gasified Hevea brasiliensis root, *Arabian J. Chem.*, 2021, **14**, 103104.

31 S. Shojaei, S. Shojaei, S. S. Band, A. A. K. Farizhandi, M. Ghoroqi and A. Mosavi, Application of Taguchi method and response surface methodology into the removal of malachite green and auramine-O by NaX nanozeolites, *Sci. Rep.*, 2021, **11**, 1–13.

32 G. R. Delpiano, D. Tocco, L. Medda, E. Magner and A. Salis, Adsorption of malachite green and alizarin red s dyes using Fe-BTC metal organic framework as adsorbent, *Int. J. Mol. Sci.*, 2021, **22**, 788.

33 H. T. T. Nguyen, T. N. Tu, M. V. Nguyen, T. H. N. Lo, H. Furukawa, N. N. Nguyen and M. D. Nguyen, Combining linker design and linker-exchange strategies for the synthesis of a stable large-pore Zr-based metal-organic framework, *ACS Appl. Mater. Interfaces*, 2018, **10**, 35462–35468.

34 V. Bon, I. Senkovska, M. S. Weiss and S. Kaskel, Tailoring of network dimensionality and porosity adjustment in Zr-and Hf-based MOFs, *CrystEngComm*, 2013, **15**, 9572–9577.

35 C. S. Nkutha, P. N. Diagboya, F. M. Mtunzi and E. D. Dikio, Application of eco-friendly multifunctional porous graphene oxide for adsorptive sequestration of chromium in aqueous solution, *Water Environ. Res.*, 2020, **92**, 1070–1079.

36 D. Chen, W. Shen, S. Wu, C. Chen, X. Luo and L. Guo, Ion exchange induced removal of Pb(II) by MOF-derived magnetic inorganic sorbents, *Nanoscale*, 2016, **8**, 7172–7179.

37 S. Liu, Z. Duan, C. He, X. Xu, T. Li, Y. Li, X. Li, Y. Wanga and L. Xua, Rapid removal of Pb^{2+} from aqueous solution by phosphate-modified baker's yeast, *RSC Adv.*, 2018, **8**, 8026–8038.

38 M. Naushad, T. Ahamad, B. M. Al-Maswari, A. A. Alqadami and S. M. Alshehri, Nickel ferrite bearing nitrogen-doped mesoporous carbon as efficient adsorbent for the removal of highly toxic metal ion from aqueous medium, *Chem. Eng. J.*, 2017, **330**, 1351–1360.

39 M. A. E. H. Hassan, L. M. A. Fayoumi and M. M. E. Jamal, Kinetic study of the discoloration of triphenylmethane dyes in function of pH, salt effect, *J. Univ. Chem. Technol. Metall.*, 2011, **46**, 395–400.

40 N. Wang, X. K. Ouyang, L. Y. Yang and A. M. Omer, Fabrication of a magnetic cellulose nanocrystal/metal–organic framework composite for removal of Pb(II) from water, *ACS Sustainable Chem. Eng.*, 2017, **5**, 10447–10458.

41 J. A. S. Costa, V. H. Sarmento, L. P. Romão and C. M. Paranhos, Adsorption of organic compounds on mesoporous material from rice husk ash (RHA), *Biomass Convers. Biorefin.*, 2020, **10**, 1105–1120.

42 C. X. Yu, K. Z. Wang, X. J. Li, D. Liu, L. F. Ma and L. L. Liu, Highly efficient and facile removal of Pb^{2+} from water by using a negatively charged azoxy-functionalized metal-organic framework, *Cryst. Growth Des.*, 2020, **20**, 5251–5260.

43 H. Wang, D. B. Jiang, J. Gu, L. Ouyang, Y. X. Zhang and S. Yuan, Simultaneous removal of phenol and Pb^{2+} from the mixed solution by zwitterionic poly(sulfobetaine methacrylate)-grafted PVBC microspheres, *Ind. Eng. Chem. Res.*, 2020, **59**, 6065–6077.

44 A. M. Omer, R. E. Khalifa, Z. Hu, H. Zhang, C. Liu and X. K. Ouyang, Fabrication of tetraethylenepentamine functionalized alginate beads for adsorptive removal of Cr(VI) from aqueous solutions, *Int. J. Biol. Macromol.*, 2019, **125**, 1221–1231.

45 A. S. Eltaweil, E. M. A. El-Monaem, G. M. El-Subruiti, M. M. A. El-Latif and A. M. Omer, Fabrication of UiO-66/MIL-101(Fe) binary MOF/carboxylated-GO composite for adsorptive removal of methylene blue dye from aqueous solutions, *RSC Adv.*, 2020, **10**, 19008–19019.

46 T. Wang, L. Zhang, C. Li, W. Yang, T. Song, C. Tang, Y. Meng, S. Dai, H. Wang, L. Chai and J. Luo, Synthesis of core-shell magnetic Fe_3O_4@poly(m-phenylenediamine) particles for chromium reduction and adsorption, *Environ. Sci. Technol.*, 2015, **49**, 5654–5662.

47 G. Vijayakumar, R. Tamilarasan and M. Dharmendirakumar, Adsorption, Kinetic, Equilibrium and thermodynamic studies on the removal of basic dye Rhodamine-B from aqueous solution by the use of natural adsorbent perlite, *J. Mater. Environ. Sci.*, 2012, **3**, 157–170.

48 A. A. Ahmad, A. T. M. Din, N. K. E. Yahaya, A. Khasri and M. A. Ahmad, Adsorption of basic green 4 onto gasified Glyricidia sepium woodchip based activated carbon: optimization, characterization, batch and column study, *Arabian J. Chem.*, 2020, **13**, 6887–6903.

49 H. N. Bhatti, A. Jabeen, M. Iqbal, S. Noreen and Z. Naseem, Adsorptive behavior of rice bran-based composites for malachite green dye: isotherm, kinetic and thermodynamic studies, *J. Mol. Liq.*, 2017, **237**, 322–333.

50 I. Ali, C. Peng, T. Ye and I. Naz, Sorption of cationic malachite green dye on phytogenic magnetic nanoparticles functionalized by 3-marcaptopropanic acid, *RSC Adv.*, 2018, **8**, 8878–8897.

51 W. Qu, T. Yuan, G. Yin, S. Xu, Q. Zhang and H. Su, Effect of properties of activated carbon on malachite green adsorption, *Fuel*, 2019, **249**, 45–53.

52 Z. Chen, H. Deng, C. Chen, Y. Yang and H. Xu, Biosorption of malachite green from aqueous solutions by Pleurotus ostreatus using Taguchi method, *J. Environ. Health Sci. Eng.*, 2014, **12**, 1–10.

53 A. S. Sartape, A. M. Mandhare, V. V. Jadhav, P. D. Raut, M. A. Anuse and S. S. Kolekar, Removal of malachite green dye from aqueous solution with adsorption technique using Limonia acidissima (wood apple) shell as low cost adsorbent, *Arabian J. Chem.*, 2017, **10**, 3229–3238.

54 Z. Shi, L. Li, Y. Xiao, Y. Wang, K. Sun, H. Wang and L. Liu, Synthesis of mixed-ligand Cu-MOFs and their adsorption of malachite green, *RSC Adv.*, 2017, **7**, 30904–30910.

55 Z. Shi, C. Xu, H. Guan, L. Li, L. Fan, Y. Wang, L. Liu, Q. Meng and R. Zhang, Magnetic metal organic frameworks (MOFs) composite for removal of lead and malachite green in wastewater, *Colloids Surf., A*, 2018, **539**, 382–390.

56 C. Li, Z. Xiong, J. Zhang and C. Wu, The strengthening role of the amino group in metal-organic framework MIL-53(Al) for methylene blue and malachite green dye adsorption, *J. Chem. Eng. Data*, 2015, **60**, 3414–3422.

57 M. S. Tehrani and R. Zare-Dorabei, Competitive removal of hazardous dyes from aqueous solution by MIL-68(Al): derivative spectrophotometric method and response surface methodology approach, *Spectrochim. Acta, Part A*, 2016, **160**, 8–18.

58 H. Liu, L. Chen and J. Ding, Adsorption behavior of magnetic amino-functionalized metal-organic framework for cationic and anionic dyes from aqueous solution, *RSC Adv.*, 2016, **6**, 48884–48895.

59 J. Abdi, M. Vossoughi, N. M. Mahmoodi and I. Alemzadeh, Synthesis of metal-organic framework hybrid nanocomposites based on GO and CNT with high adsorption capacity for dye removal, *Chem. Eng. J.*, 2017, **326**, 1145–1158.